

The luminosity dependence of thermally-driven disc winds in X-ray binaries

Nick Higginbottom,¹★ Christian Knigge¹, Knox S. Long^{2,3}, James H. Matthews⁴ and Edward J. Parkinson¹.

¹*School of Physics and Astronomy, University of Southampton, Highfield, Southampton, SO17 1BJ, UK*

²*Space Telescope Science Institute, 3700 San Martin Drive, Baltimore, MD, 21218, USA*

³*Eureka Scientific Inc., 2542 Delmar Avenue, Suite 100, Oakland, CA, 94602-3017, USA*

⁴*University of Oxford, Astrophysics, Keble Road, Oxford OX1 3RH, UK*

⁵*School of Mathematics and Physics, Queen's University Belfast, University Road, Belfast BT7 1NN, UK*

Accepted XXX. Received YYY; in original form ZZZ

ABSTRACT

We have carried out radiation-hydrodynamic simulations of thermally-driven accretion disc winds in X-ray binaries. Our main goal is to study the luminosity dependence of these outflows. The simulations span the range $0.04 \leq L_{\text{acc}}/L_{\text{Edd}} \leq 1.0$ and therefore cover most of the parameter space in which disc winds have been observed. We find that (i) the wind *efficiency* always remains approximately constant, $\dot{M}_{\text{wind}}/\dot{M}_{\text{acc}} \simeq 2$; (ii) the wind velocity increases with luminosity, roughly as $v \propto L_{\text{acc}}^{1/4}$; (iii) the large-scale wind geometry is quasi-spherical, but observable absorption features are preferentially produced along high-column equatorial sightlines; (iv) with increasing luminosity, detectable high-ionization absorption features are produced at lower inclinations. In order to illustrate the observational signatures of such outflows, we also present synthetic Fe xxv and Fe xxvi absorption line profiles for our simulated disc winds.

Key words: Accretion discs – hydrodynamics – methods:numerical – stars:winds – X-rays:binaries

1 INTRODUCTION

Signatures of outflowing gas have been observed in essentially all types of disk-accreting astrophysical systems, from protostars, cataclysmic variables and X-ray binaries to Seyfert Galaxies and Quasars. Highly collimated fast jets are often the most spectacular type of outflow from these systems. However, less collimated, slower and more highly mass-loaded disk winds are at least as common and can actually have a more significant impact, both on the environments of these systems and on the accretion flow itself.

X-ray binaries (XRBs) are systems in which secondary star transfers mass to a compact primary (either a black hole or a neutron star) via an accretion disk. They are excellent laboratories in which to study the accretion physics, with lessons learned from XRBs often finding application also in AGN and other systems) (Maccarone et al. 2003; Falcke et al. 2004; K rding et al. 2006; ?; ?; ?; ?; ?; ?; ?). In particular, XRBs exhibit dramatic changes in their spectra and luminosity over timescales on the order of days (e.g. Sobczak et al. 1999; Park et al. 2004), which can be linked to changes in the

nature of the accretion flow (e.g. Nowak 1995; Fender & Belloni 2012). Disk winds are seen when systems are in the “high-soft” state, during which the accretion disk is thought to extend all the way to the central compact object (Ponti et al. 2012, although see Homan et al. 2016). Disc wind signatures are not generally observed in the “low-hard” state, during which the inner disk appears to be truncated, and the X-ray emission is dominated by a Comptonised corona. This suggests that disc winds might play a role in regulating – and perhaps triggering – state changes in XRBs. In fact, for sufficiently high mass-loss rates, disc winds are *expected* to destabilize a steady accretion flow through the disc (Shields et al. 1986).

We are therefore interested in developing a theoretical model for these disk winds, with an eye to predicting their mass-loss rates and hence testing the possibility that they are indeed responsible for state changes. Unfortunately, even the basic driving mechanism for these disk winds remains a topic of much debate and active research. However, broadly speaking, there are three main contenders – radiation driving, thermal driving, and magneto-centric driving.

The first mechanism, radiation driving, involves the transfer of momentum from the radiation field to outflowing matter. This transfer can take place via Compton scattering or via the scattering of (mainly UV) photons by bound-bound transitions. If the ionisation

★ E-mail: nick_higginbottom@fastmail.fm

state of the gas is favourable, the latter “line-driving” mechanism can produce a radiation pressure more than 1000× higher than that due to Compton scattering (Castor et al. 1975; ?). In X-ray binaries, the observed absorption lines suggest that the outflow is highly ionised (e.g. Kallman et al. 2009; Allen et al. 2018), with an ionization parameter $\xi \geq 3$ (Díaz Trigo & Boirin 2016). In such an environment, line-driving is unlikely to be important. However, the luminosity of some XRBs can approach or even exceed the Eddington limit, so radiation driving via Compton scattering alone may be sufficient to drive – or at least affect – the outflow.

The second mechanism, thermal driving, produces outflows whenever gas is heated to a temperature at which the thermal velocity exceeds the local escape velocity. In this situation, mass-loss is inevitable. This mechanism is particularly attractive in X-ray binaries, where the high-energy radiation emitted close to the accretor can irradiate the outer disk, producing a high-temperature surface layer in which thermal speeds can exceed the escape velocity. As a rule of thumb, thermal winds might be expected to arise at or just inside the Compton Radius (R_{IC}) – the radius at which gas at the Compton temperature (T_C – the temperature at which the Compton heating and cooling rates balance) for a given source SED corresponds to a thermal velocity in excess of the escape velocity (Begelman et al. 1983). More specifically, R_{IC} is given by

$$R_{IC} = \frac{GM_{BH}\mu m_H}{k_B T_C}, \quad (1)$$

where M_{BH} is the mass of the central object, μ is the mean molecular mass (which we set to 0.6), and the other symbols have the usual meaning. For our SED, $T_C = 1.4 \times 10^7$ K, so $R_{IC} = 4.82 \times 10^{11}$ – about 4.6×10^5 gravitational radii.

The third proposed mechanism is that of magneto-centrifugal driving. Observations of the disk-wind in GRO J1655-40 in a peculiar ‘hypersoft’ state suggested that the wind in that case arose well inside R_{IC} . In such a case the existence of a thermal wind is harder to justify and magneto-centrifugal driving has been suggested as an alternative driving mechanism (Stone & Norman 1992; Miller et al. 2006, 2008; Kallman et al. 2009, but also see Netzer 2006; Uttley & Klein-Wolt 2015; Shidatsu et al. 2016). Since magnetic fields are essential in the evolution of accretion disks, it is not unreasonable to expect such winds to exist. In such a wind, ionized material is loaded onto magnetic field lines leaving the accretion disk, and via a process of angular momentum conservation, the material is accelerated as it moves out along the field lines, like beads on a wire.

Most likely, all three mechanisms are at play, perhaps changing their importance depending on the geometry and accretion state of the source in question. Of the three mechanisms, thermal driving is particularly interesting in X-ray binaries because it is almost certain to operate on some level wherever there is strongly heated gas and a disk of sufficient radial extent that hot gas can escape. Indeed, this mechanism might not only be important in X-ray binaries but also in protoplanetary systems (e.g. Owen et al. 2012) and AGN (e.g. Bu & Yang 2018).

The existence of thermally driven outflows from accretion disks has been postulated since such disks were themselves first considered (Shakura & Sunyaev 1973). More detailed theoretical treatment of thermal winds (Begelman et al. 1983) suggested that the mass-loss could be sufficient to destabilise the disk (Shields et al. 1986). As computer power improved, more detailed hydrodynamic simulations (Woods et al. 1996; Netzer 2006; Luketic et al. 2010; Higginbottom & Proga 2015) have provided support for the earlier predications of large mass-loss rates and also showed that thermal

winds could provide a source of observed blue shifted absorption lines.

Although very large mass-loss rates are possible through thermal winds, the actual rate is very dependant on the details of the heating/cooling rates (Higginbottom et al. 2017). These in turn depend critically on the source SED (Dyda et al. 2017) and any attenuation effect between the source and the wind launching region. Higginbottom et al. (2018, hereafter H18) presented a radiation-hydrodynamic simulation which took account of this attenuation by coupling the radiative transfer code `PYTHON` to the hydrodynamics code `ZEUS` and found that there was still an appreciable outflow, with about two and a half times as much material outflowing as was required to produced the observed luminosity through accretion. In addition, reasonable agreement was found between Lyman α lines of helium and hydrogen like iron generated from the simulation and those seen in *Chandra* observations of the LMXB GRO J1655-40 in the soft-intermediate state.

That simulation was for a luminosity of 4 per cent of the Eddington luminosity (L_{Edd}) for a 7 solar mass central black hole but disk winds have been observed in systems with luminosities up to or even slightly exceeding L_{Edd} (Ponti et al. 2012, hereafter P12). Observations suggest that the wind efficiency (mass loss rate divided by mass accretion rate) may increase with luminosity, (P12, although this relationship is driven by observations of a single exceptional source) whilst recent theoretical work suggests that the wind efficiency tends to a constant value (Done et al. 2018, hereafter D18).

Here, we extend our radiation hydrodynamic simulations to higher luminosities in order to investigate the effect on mass loss rate and velocity in the resulting outflows. As discussed in Section 2, we use the same technique as H18 with slight modifications for varying the luminosity. We then present our results in Section 3 before making comparisons to observations in Section 4.

2 METHOD

As in H18, we use an operator splitting radiation-hydrodynamic method to treat the propagation of radiation from a central source through the wind. We use the hydrodynamic code `ZEUS` (Stone & Norman 1992, extended by Proga et al. 2000), coupled to our own ionization and radiative transfer code `PYTHON` (Long & Knigge 2002, extended by Higginbottom et al. 2013 and Matthews et al. 2015).

Since thermal winds are expected to arise at or just inside R_{IC} , which is independent of the source luminosity, we leave the simulation geometry unchanged from H18, and simply increase the luminosity. We use the same logarithmic grid, the parameters of which are given in the upper part of Table 1. The mid-plane of the simulation space is set up with a constant density boundary condition, forming a mass reservoir for any resulting outflow. The value of this constant density is important, since the wind is generated when the ionization parameter reaches the critical value $\xi_{cool,max}$ which represents the maximum ionization parameter for gas on the ‘cool branch’ of the thermal stability curve. Gas with $\xi < \xi_{cool,max}$ has a stable temperature of a few tens of thousands K where line/recombination cooling balances photoionization heating.

At higher ionization parameters, the gas becomes thermally unstable and heats up rapidly. This heating causes expansion and a wind is driven. We refer to the part of the wind where this acceleration occurs as the acceleration zone. In the optically thin limit

Luminosity (L_{edd})	0.04	0.1	0.3	0.6
Physical Parameters				
M_{BH} (M_{\odot})	7	7	7	7
T_x (10^7 K)	5.6	5.6	5.6	5.6
L_x (10^{37} ergs s^{-1})	3.3	8.25	24.75	49.5
\dot{M}_{acc} (10^{17} ergs s^{-1})	4.42	11.1	33.2	66.3
$\log(\xi_{\text{cold,max}})$	1.35	1.35	1.35	1.35
$T_{\text{eq}}(\xi_{\text{cold,max}})$ (10^3 K)	50.7	50.7	50.7	50.7
ρ_0 (10^{-12} g cm^{-3})	16.0	40	120	240
R_{IC} (10^{11} cm)	4.82	4.82	4.82	4.82
Derived wind properties				
$V_r(\text{max}, \theta > 60^\circ, \text{ km s}^{-1})$	259	374	533	642
$T(\text{max}, \theta > 60^\circ, r > R_{\text{IC}}, 10^6 \text{ K})$	2.8	3.8	5.3	6.7
$N_{\text{H}}(70^\circ)$ (10^{22} cm^{-2})	2.0	4.0	8.3	13
$N_{\text{H}}(80^\circ)$ (10^{22} cm^{-2})	4.2	8.4	16	25
Angle for 5eV EW Fe xxv	73°	72°	77°	77°
Angle for 5eV EW Fe xxvi	68°	62°	60°	60°
$\dot{M}_{\text{wind,outer}}$ (10^{18} g s^{-1})	1.1	2.7	6.7	12.7
$\dot{M}_{\text{wind,outer}}(\dot{M}_{\text{acc}})$	2.5	2.4	2.0	1.9
$0.5\dot{M}V_r^2$ (10^{32} erg s^{-1})	4.2	21.3	109	310

Table 1. Parameters adopted in the simulations, along with key properties of the resulting outflows.

one can set the mid-plane density so that gas at the mid-plane has exactly the right ionization parameter. This means that the acceleration zone occurs in the cells directly above the mid-plane, avoiding including static material in the simulation, and thus maximizing the resolution in the acceleration zone.

In the simulations presented here attenuation of the radiation is treated fully and it is therefore not possible to compute the ionization parameter for a given cell a-priori since it depends not only on the local density but also on the density of the developing wind along the sightline back to the source. We therefore set the mid-plane density using the optically thin ionisation parameter, finding that a small wedge of static material does form due to optical depth effects. However the extent of this does not significantly affect the resolution in the acceleration zone. The mid-plane densities we have used are given in Table 1. They are proportional to the source luminosity, thereby preserving the same ionization parameter (in the optically thin approximation).

All other aspects of the simulation are identical to that described by H18, including a truncation of the mid-plane density boundary condition at $R = 2R_{\text{IC}}$.

3 RESULTS

We have computed disk-wind models for central source luminosity $L = 0.1 L_{\text{Edd}} - 1.0 L_{\text{Edd}}$ in steps of $0.1 L_{\text{Edd}}$. In each case, the simulations reach stable states, with static disk-like wedges forming at the base of the simulation as seen in H18. The reason for this structure is attenuation of the radiation through the disk. So, if a cell at a given angle has just the right conditions to launch a wind, the cell behind it will be slightly obscured and so on until at a certain radius the radiation is attenuated to the point at which a wind is launched from the next theta cell 'up'. This gives rise to a thin, slightly convex disk structure.

Because we increase the mid-plane density in proportion to the luminosity in order to try and maintain a fixed ionization parameter

at the base of the wind, the shape of the disk structure slightly changes as the luminosity increases. In all cases, at the inner radial edge, the disk/wind interface occurs at around 89° from the z-axis (i.e. 1° above the mid-plane). For the original $0.04L_{\text{Edd}}$ simulation, the angle at which the interface occurs decreases to about 88° at the outer edge, whereas for the L_{Edd} simulation, the interface is about a degree further from the midplane at 87° .

Density contour plots for some of the resulting outflows are shown in Figure 1. We concentrate here, and in the rest of the results/discussion sections, on the calculations using luminosities up to 60 per cent of L_{Edd} . This is because we do not treat radiation driving, a process that would become increasingly important as the luminosity approaches L_{Edd} . It is clear from these images that the velocity of the outflows increases with luminosity, as does the density in the wind. Some useful parameters showing this are given in the lower part of Table 1. As one would expect, the mass-loss rate through the outer boundary, which is essentially a function of these two parameters also increases with luminosity. We will discuss this further in the next section.

The outflow is approximately spherical, becoming more-so as the luminosity increases. However observationally the wind is equatorial because the density distribution is concentrated towards the mid-plane. Table 1 contains data which show the inclination angle at which the equivalent width of two simulated line profiles (see Section 4.3 for more details) first exceed 5eV, a reasonable value for detectability. For the low luminosity case, this is around 70° for both Fe xxv and Fe xxvi.

As the luminosity increases the angle at which the lines are seen moves towards the equator for the Fe xxv feature and towards the pole for Fe xxvi as the ionization state changes.

4 DISCUSSION

4.1 Mass-loss rates

The mass-loss rates ($\dot{M}_{\text{wind,outer}}$) listed in Table 1 increase as the luminosity of the central source increases. However when we compare these values to the implied accretion rate (\dot{M}_{acc}) we find that $\dot{M}_{\text{wind,outer}} \approx 2\dot{M}_{\text{acc}}$ for all cases. This constant 'wind efficiency' is similar to that found in the analysis carried out by Done et al. (2018) who found that for a disk of our size ($R_{\text{out}} = 2R_{\text{IC}}$) and a Compton temperature very close to ours the wind efficiency peaked at just over two for a luminosity close to our lowest luminosity. They then see the efficiency decrease slowly with increasing luminosity, always remaining above one. Our wind efficiencies are slightly larger than theirs, which is interesting since we neglect any radiation driving effects, which they include via an approximate correction.

The wind efficiency for a range of observed XRB winds is given by Ponti et al. (2012). It is instructive to compare our results with these observations. Figure 2 shows this comparison, with the black symbols referring to the observations and the red stars showing the results of these simulations.

At first sight, our prediction of a constant wind efficiency does not appear to agree with the observations, which appear to suggest an increase of wind efficiency with luminosity. However, the increase in wind efficiency with luminosity is largely driven by observations of just one source - GRS 1915 +105. This is an exceptional source, which has been accreting close to the Eddington limit since its discovery in 1992 never entering quiescence (Castro-Tirado et al. 1994; Court et al. 2017). It also exhibits unusual SEDs, not corresponding to the normal high/soft, low/hard spectral states (Zoghbi et al.

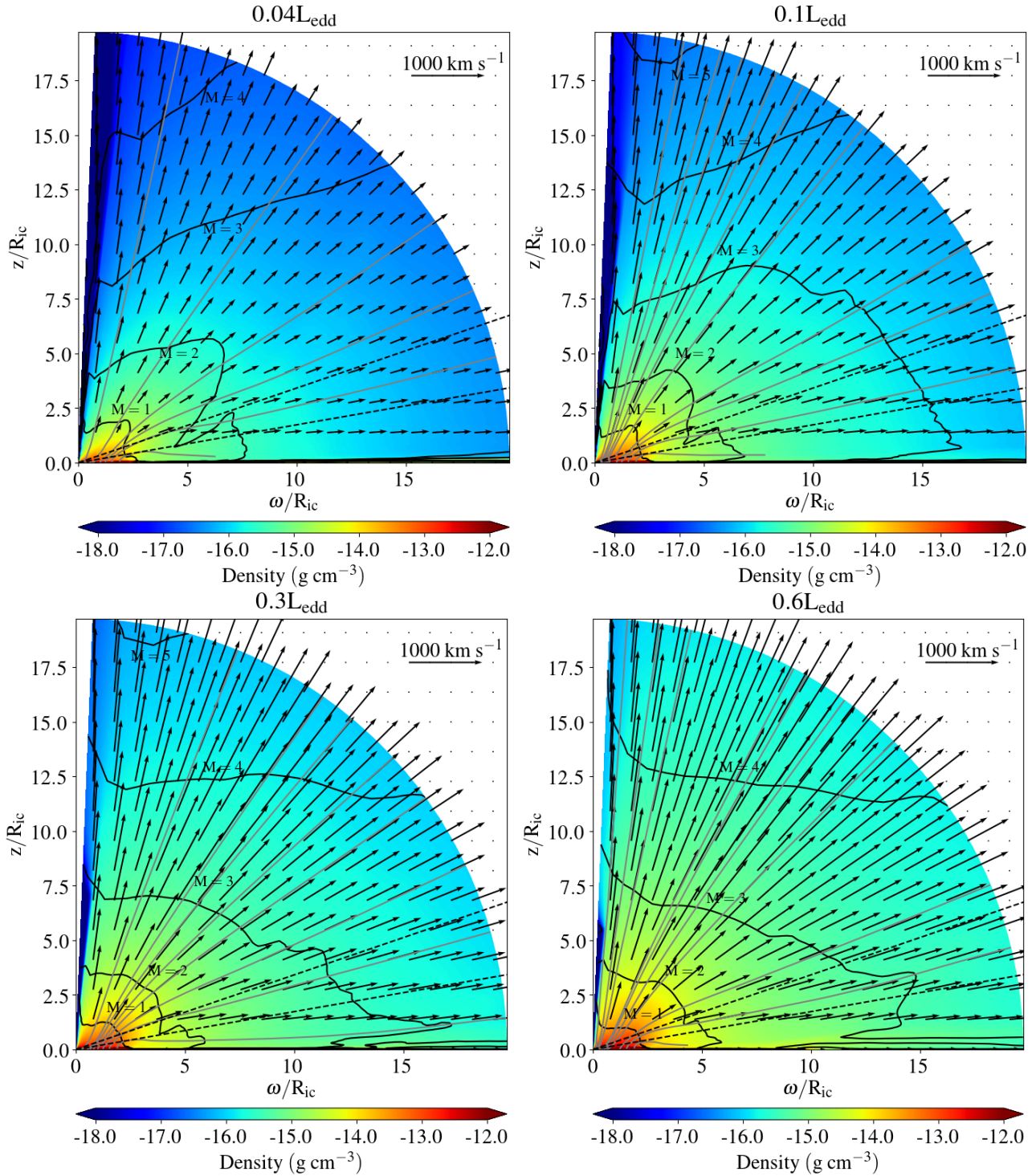


Figure 1. The density (colours) and velocity structure (arrows) of the stable final states for four different luminosities. Grey lines show streamlines, and the black line shows the location of the Mach surfaces. The two dotted lines show the location of the 70° and 80° sightlines.

2016). Finally, with an orbital period of 34 days (Casares & Jonker 2014) this is by far the largest system - and could perhaps host a significantly larger accretion disk than we include in our model. This complex source requires more detailed analysis and modelling which is beyond the scope of this study. Setting aside the observations of this source, the rest show reasonable consistency with wind

efficiency around two over a significant range of luminosities, as seen in the simulations.

4.2 Comparison to B83 calculations

A useful way of categorising different classes of thermally driven winds was introduced by (Begelman et al. 1983, hereafter B83),

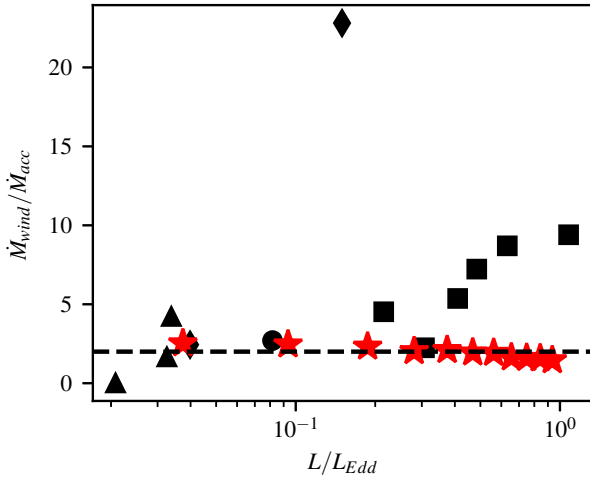


Figure 2. $M_{\text{wind}}/M_{\text{acc}}$ vs. luminosity based upon figure 5 in Ponti et al. (2012). Black symbols are empirical values obtained from *Chandra* HETG data for several LMXBs. The symbols refer to the specific object each measurement refers to (triangles = H1743-322; circles = 4U 1640-47; squares = GRS 1915+105; diamonds = GRO J1655-40). The red stars represent the results of the simulations presented here, and the dotted line is at $M_{\text{wind}}/M_{\text{acc}}=2.0$.

and further developed by (Woods et al. 1996, hereafter W96). The diagram from B83 is reproduced in Figure 3. The vertical axis is the luminosity of the central source in units of the ‘critical luminosity’ defined as

$$L_{\text{crit}} = 0.03 T_{C,8}^{-1/2} L_{\text{Edd}} \quad (2)$$

where $T_{C,8}$ is the Compton temperature in units of 10^8 K, whilst the horizontal axis is the radius on the disk where streamline arises normalised to the Compton radius.

The different regions designate different types of outflow or static atmosphere, and are a consequence of how quickly the plasma is heated. The regions in the lower half of the Figure heat slowly whilst regions in the upper half heat rapidly to the Compton temperature. The regions on the right hand side are where gas at the Compton temperature would be expected to escape, whilst on the left hand side the gas is gravitationally bound and so forms an atmosphere rather than a wind. In regions B and C, the gas flows outwards too quickly to be heated to the Compton temperature. In region B the gas temperature still exceeds the temperature needed to escape at the radius at which it is launched, whereas in region C it does not even reach that temperature and so the gas remains gravitationally bound.

B83 found that there was not a clear dividing line between bound and unbound solutions at $\omega = R_{\text{IC}}$. W96 found that a more reasonable location for this cutoff was $\omega = 0.1 R_{\text{IC}}$. Our 4 per cent simulation represents about $0.5 L_{\text{crit}}$ and is shown on Figure 3 as the lowest horizontal dashed line. The 10 per cent simulation (next horizontal line up) has a luminosity just below L_{crit} and the two higher luminosity cases are above L_{crit} . We would therefore expect to see a clear difference between the lowest luminosity case and the two higher cases with gas impulsively heated to the Compton temperature in the latter. However, although the outflowing gas gets hotter as the luminosity increases in no case does it approach T_{IC} . In fact we see that, as the gas expands and accelerates away, adiabatic

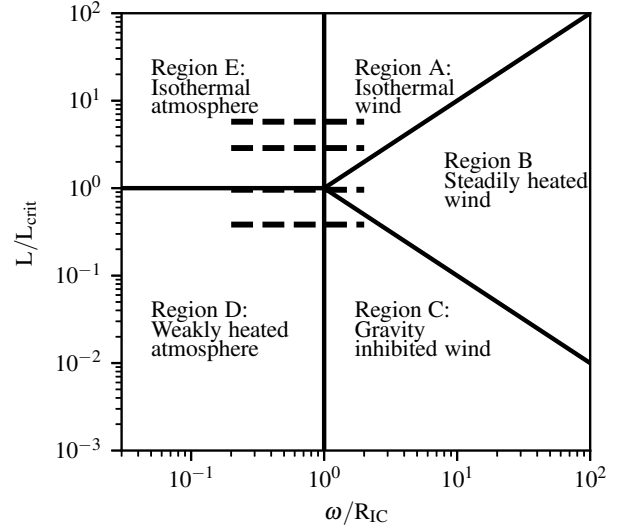


Figure 3. Regions of different wind solutions after Begelman et al. (1983). The horizontal dashed lines represent the luminosity and disk extent of the simulations in H18 (lowest line) and those presented here

cooling increases quickly and balances Compton heating and X-ray heating in much of the wind. The gas heats up initially, reaching a peak temperature at a distance of about R_{IC} along the streamline of between about 1×10^6 K for the low luminosity case and 6×10^6 K for $L = L_{\text{Edd}}$. The temperature then starts dropping.

The Bernoulli parameter is given by $Be \equiv v^2 + \gamma P/(\gamma - 1)\rho - GM_{bh}/r$, where the first term is the kinetic energy of the gas with velocity v , the second term is the gas enthalpy and the third term is the gravitational potential. Be is negative at the streamline roots; the gas is gravitationally bound at this point. It then increases along all streamlines despite a slow decrease in gas enthalpy and becomes positive. This demonstrates that the heating is sufficient to provide the work to lift the gas out of the potential well - and also accelerate the gas producing a significant increase in kinetic energy along the streamlines. The kinetic energy also includes a significant component due to the rotational velocity - angular momentum is conserved along streamlines so the rotational velocity drops as the gas moves outward.

4.3 Line Shape

We have also computed some simulated absorption line profiles. Firstly, in Figure 4 we show the Fe xxv Lyman α transition at 1.85 \AA for a sightline of 80° . This is calculated using the same ray tracing technique as discussed by Higginbottom & Proga (2015). The equivalent width (EW) is very similar for all the lines (because they are all saturated) at about 5-6 eV.

There are two interesting observations to be made from this plot. Firstly, the maximum velocity seen in the line increases with luminosity. Secondly, there is a notable difference between the line two lower luminosity profiles and the higher pair. All lines exhibit some absorption at about $+100 \text{ km s}^{-1}$, due to thermal broadening of absorption from stationary or slow moving material. However for the 4 per cent and 10 per cent cases the feature is almost black at 0 km s^{-1} indicating the presence of more slow moving material than in the 30 and 60 per cent cases. As discussed in Section 4.2, the two

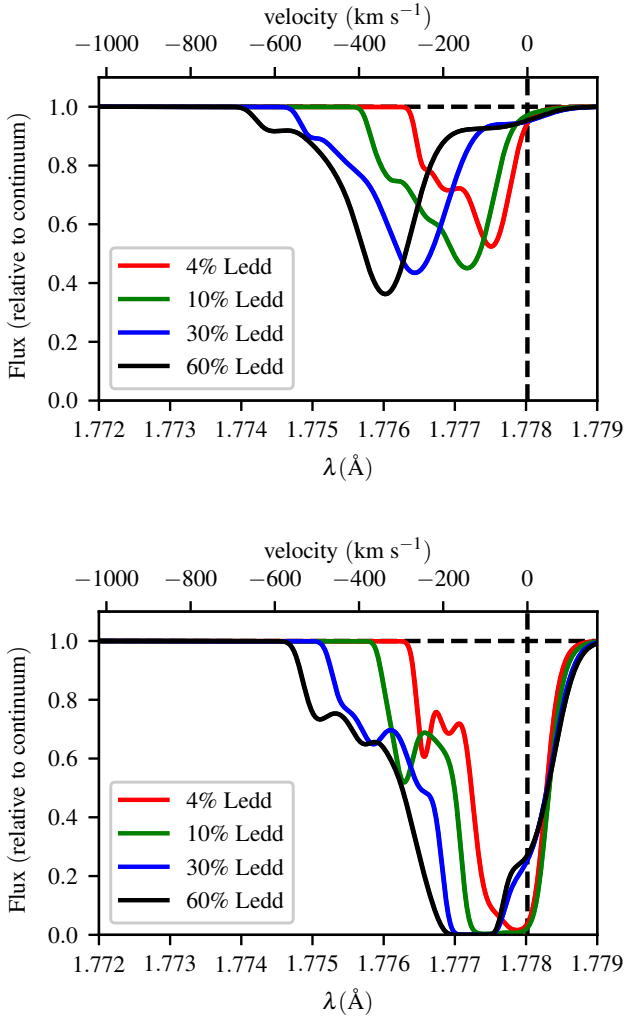


Figure 4. Simulated line profile for the stronger line of the Fe xxvi Lyman α doublet at 1.778 Å, as viewed from $i = 60^\circ$ (upper panel) and $i = 60^\circ$ (lower panel) for a range of luminosities.

higher luminosity runs are in the “isothermal” part of Figure 3 and the gas in these cases would be expected to be more impulsively heated. Whilst the gas does not reach the Compton temperature in either case, the shape of the lines does point to a faster heating process and a quicker acceleration.

Another line commonly seen in XRB winds is the Lyman α resonance line of Fe xxvi which is actually a doublet with components at 1.778 Å and 1.783 Å. The ray traced absorption profile for this feature is given as the thin lines in Figure 5. The absorption profile as a function of velocity in each of the two lines is almost identical to that seen in the Fe xxv feature shown in Figure 4 but these features are slightly less saturated and hence there is a range of EWs for the doublet, ranging from -8 eV for the 4% L_{Edd} run to -16 eV for the 60% luminosity. The run at the Eddington luminosity has an EW of almost 20eV, but this should be treated with caution because of the lack of radiation driving in our simulation. If radiation driving is important as would be expected then one would expect a significantly larger EW.

The current generation of X-ray spectrometers are unable to

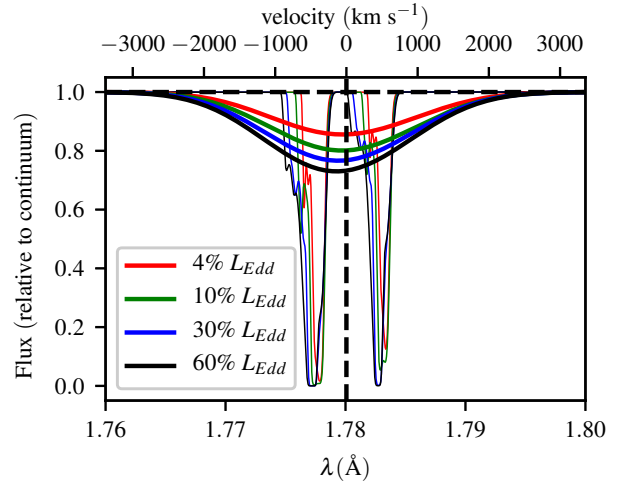


Figure 5. Simulated line profile for the Fe xxvi Lyman α doublet, as viewed from $i = 80^\circ$ for a range of luminosities (thin lines) and also smoothed with a Gaussian to represent the appearance when observed with the *Chandra* HETG with a resolution of 0.012 Å (thick lines)

split this feature into its components; for example the wavelength resolution of the *Chandra* HETG is 0.012 Å compared to the feature spacing of 0.005 Å. Therefore the feature is always observed as a single line. The heavy lines in Figure 5 show the line pair smoothed by a Gaussian to reproduce the appearance of this line through the *Chandra* HETG.

The EW of lines observed in X-ray binary disk winds are mostly around 10-30eV Ponti et al. (2012), similar to the values we obtain here. The velocities are higher however, ranging between about 400-3000 km s⁻¹ Díaz Trigo & Boirin (2016). It is possible that the including of continuum driving would accelerate the winds to higher velocities. This would tend to increase the EW since the lines in our simulations are black in places, and this dense gas would be more distributed in velocity space.

4.4 Kinetic Luminosity

Whilst the mass loss is of interest when considering how the wind could affect the accretion flow through the disk, it is also interesting to consider what (if any) effect the wind could have on the surroundings. The kinetic energy carried by the wind is a good measure of this, and so we calculate this via a simple summation around the outer edge of the domain.

The results are plotted in Figure 6 together with observed values from Ponti et al. (2016) for the same sources as plotted in Figure 2. Taking into account the flare of the disk (which is 4° for the lowest luminosity rising to 6° for the $L = L_{\text{Edd}}$ run the efficiency of conversion from intercepted radiative luminosity into kinetic energy is about 0.1 per cent for our runs with $L \geq 0.2L_{\text{Edd}}$. For the two lower luminosity runs, the efficiency is lower, at 0.04 per cent for $0.04L_{\text{Edd}}$ and 0.06 per cent for $0.1L_{\text{Edd}}$. Interestingly these are the two runs where the luminosity is below L_{crit} .

The flare seen in our simulations is a function of the radiative transfer process as discussed earlier, and we do not include any underlying flare in the accretion disk. It has been shown that at high Eddington fractions, accretion disks tend to puff up to larger scale heights (Abramowicz et al. 1988; Okuda et al. 2005, but also see

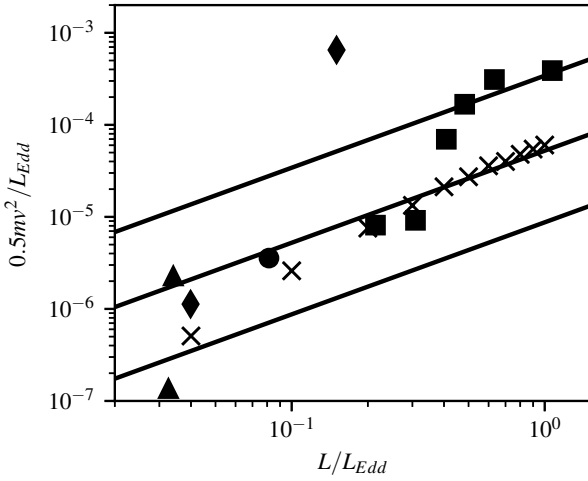


Figure 6. Kinetic energy transported by the wind as a function of source luminosity, both normalised to the Eddington luminosity. Crosses are for this work, the other symbols represent data from Ponti et al. (2016), the symbols code for different sources as in Figure 2. The diagonal lines show theoretical calculations of kinetic luminosity assuming a 0.1 per cent conversion from luminosity to kinetic energy for disks with 1°, 6° and 40° total flare.

Lasota et al. 2016) and so we would expect such a disk to intercept a greater fraction of the incoming radiation. This could explain the way in which the observed kinetic energy flux dramatically increases at luminosities greater than 30 per cent Eddington. The diagonal lines show the relationship between radiative and kinetic luminosity for 1°, 6° and 40° total disk flare angles. We see that as expected our results tend to the 6° line, and if the efficiency is the same at all higher luminosities we would require a disk opening angle of 40° to explain the high luminosity results. It is possible that the efficiency could also increase when radiation driving is included.

4.5 Effect of radiation driving

As the luminosity increases, one should include the effects of radiation pressure on the simulation. For such a relatively hard SED, the plasma above the disk will be largely ionized, and so electron pressure would be the only radiation pressure one would expect. The effect can be thought of as effectively a reduction in the inner radius at which a wind is launched. Done et al. (2018) give this correction as

$$\bar{R}_{IC} \approx R_{IC} \left(1 - \frac{L}{0.71 L_{Edd}} \right) \quad (3)$$

which means that the wind can be launched from all radii at a luminosity of $0.71 L_{Edd}$. This in turn means that our mass loss rates will be a lower bound for luminosities approaching or exceeding this value. We can make a rough estimate of the effect on the mass-loss rate of including radiation driving by noting that for the 60 per cent and 100 per cent Eddington runs, the mass-loss rate per unit area is approximately proportional to $R^{-1.5}$. If all the radii interior to where the wind current arises were to follow this relationship, then the mass-loss would increase by a factor of about 1.5. We might also expect somewhat higher velocities in the outflow, due to the additional force, which could also increase the efficiency

of conversion from radiative luminosity into kinetic luminosity as previously mentioned. We are planning to include this effect in our next set of simulations.

5 SUMMARY

Thermal driving is an attractive mechanism to explain the outflows observed in several X-ray binaries seen at high inclinations. We have previously demonstrated that the outflow seen in the soft-intermediate state of GRO J1655-40 could be plausibly modelled by a thermal wind, and here we extend that work to higher luminosities. We find

- As the luminosity (and therefore accretion rate) increases, so does the mass-loss rate through the wind. The ratio between the two, $\dot{M}_{wind}/\dot{M}_{acc}$ or the wind efficiency, tends to a constant value of around 2. This is in agreement with previous theoretical studies and also observations.
- At the luminosity increases, the maximum blue shifted velocities seen in a simulated Fe xxv and Fe xxvi absorption lines increases. There is also less material at low velocities as the material is more impulsively heated.
- The kinetic energy transported by the wind also increases with luminosity however; the efficiency of conversion from radiative luminosity to kinetic luminosity is about 0.1 per cent. Differences between our predicted kinetic energy and observations could be explained by either a difference in efficiency (possibly due to continuum driving) or an increased underlying disk flare at high luminosities.

These simulations do not include the effects of radiation driving, which may become important at higher luminosities.

6 ACKNOWLEDGEMENTS

Calculations in this work made use of the Iridis4 Supercomputer at the University of Southampton. NH and CK acknowledge support by the Science and Technology Facilities Council grant ST/M001326/1. KSL acknowledges the support of NASA for this work through grant NNG15PP48P to serve as a science adviser to the Astro-H project, JHM is supported by STFC grant ST/N000919/1 and SAS is supported by STFC through grant, ST/P000312/1.

REFERENCES

- Abramowicz M. A., Czerny B., Lasota J. P., Szuszkiewicz E., 1988, *ApJ*, 332, 646
 Allen J. L., Schulz N. S., Homan J., Neilsen J., Nowak M. A., Chakrabarty D., 2018, *ApJ*, 861, 26
 Begelman M. C., McKee C. F., Shields G. A., 1983, *ApJ*, 271, 70
 Bu D.-F., Yang X.-H., 2018, *MNRAS*, 476, 4395
 Casares J., Jonker P. G., 2014, *Space Sci. Rev.*, 183, 223
 Castor J. I., Abbott D. C., Klein R. I., 1975, *ApJ*, 195, 157
 Castro-Tirado A. J., Brandt S., Lund N., Lapshov I., Sunyaev R. A., Shlyapnikov A. A., Guziy S., Pavlenko E. P., 1994, *ApJS*, 92, 469
 Court J. M. C., Altamirano D., Pereyra M., Boon C. M., Yamaoka K., Belloni T., Wijnands R., Pahari M., 2017, *MNRAS*, 468, 4748
 Díaz Trigo M., Boirin L., 2016, *Astronomische Nachrichten*, 337, 368
 Done C., Tomaru R., Takahashi T., 2018, *MNRAS*, 473, 838
 Dyda S., Dannen R., Waters T., Proga D., 2017, *MNRAS*, 467, 4161
 Falcke H., Kording E., Markoff S., 2004, *A&A*, 414, 895
 Fender R., Belloni T., 2012, *Science*, 337, 540
 Higginbottom N., Proga D., 2015, *ApJ*, 807, 107

- Higginbottom N., Knigge C., Long K. S., Sim S. A., Matthews J. H., 2013, MNRAS, 436, 1390
- Higginbottom N., Proga D., Knigge C., Long K. S., 2017, ApJ, 836, 42
- Higginbottom N., Knigge C., Long K. S., Matthews J. H., Sim S. A., Hewitt H. A., 2018, MNRAS, 479, 3651
- Homan J., Neilsen J., Allen J. L., Chakrabarty D., Fender R., Fridriksson J. K., Remillard R. A., Schulz N., 2016, ApJ, 830, L5
- Kallman T. R., Bautista M. A., Goriely S., Mendoza C., Miller J. M., Palmeri P., Quinet P., Raymond J., 2009, ApJ, 701, 865
- Körding E. G., Jester S., Fender R., 2006, MNRAS, 372, 1366
- Lasota J.-P., Vieira R. S. S., Sadowski A., Narayan R., Abramowicz M. A., 2016, A&A, 587, A13
- Long K. S., Knigge C., 2002, ApJ, 579, 725
- Luketic S., Proga D., Kallman T. R., Raymond J. C., Miller J. M., 2010, ApJ, 719, 515
- Maccarone T. J., Gallo E., Fender R., 2003, MNRAS, 345, L19
- Matthews J. H., Knigge C., Long K. S., Sim S. A., Higginbottom N., 2015, MNRAS, 450, 3331
- Miller J. M., Raymond J., Fabian A., Steeghs D., Homan J., Reynolds C., van der Klis M., Wijnands R., 2006, Nature, 441, 953
- Miller J. M., Raymond J., Reynolds C. S., Fabian A. C., Kallman T. R., Homan J., 2008, ApJ, 680, 1359
- Netzer H., 2006, ApJ, 652, L117
- Nowak M. A., 1995, PASP, 107, 1207
- Okuda T., Teresi V., Toscano E., Molteni D., 2005, MNRAS, 357, 295
- Owen J. E., Clarke C. J., Ercolano B., 2012, MNRAS, 422, 1880
- Park S. Q., et al., 2004, ApJ, 610, 378
- Ponti G., Fender R. P., Begelman M. C., Dunn R. J. H., Neilsen J., Coriat M., 2012, MNRAS, 422, 11
- Ponti G., Bianchi S., Muñoz-Darias T., De K., Fender R., Merloni A., 2016, Astronomische Nachrichten, 337, 512
- Proga D., Stone J. M., Kallman T. R., 2000, ApJ, 543, 686
- Shakura N. I., Sunyaev R. A., 1973, A&A, 24, 337
- Shidatsu M., Done C., Ueda Y., 2016, ApJ, 823, 159
- Shields G. A., McKee C. F., Lin D. N. C., Begelman M. C., 1986, ApJ, 306, 90
- Sobczak G. J., McClintock J. E., Remillard R. A., Bailyn C. D., Orosz J. A., 1999, ApJ, 520, 776
- Stone J. M., Norman M. L., 1992, ApJS, 80, 753
- Uttley P., Klein-Wolt M., 2015, MNRAS, 451, 475
- Woods D. T., Klein R. I., Castor J. I., McKee C. F., Bell J. B., 1996, ApJ, 461, 767
- Zoghbi A., et al., 2016, ApJ, 833, 165
- ()

This paper has been typeset from a \LaTeX file prepared by the author.